

# Gradient-Based Predictive Pulse Pattern Control of Medium-Voltage Drives—Part I: Control, Concept and Analysis

Mirza Abdul Waris Begh, *Student Member, IEEE*, Petros Karamanakos, *Senior Member, IEEE*, and Tobias Geyer, *Fellow, IEEE*

**Abstract**—This paper proposes a control and modulation strategy for medium-voltage (MV) drives that exhibits excellent steady-state and transient behavior. Specifically, optimized pulse patterns (OPPs) and direct model predictive control (MPC) are employed so that the associated advantages of both, such as minimum stator current total demand distortion (TDD) and fast transients, respectively, are fully exploited. To do so, the current reference trajectory tracking and modulation problems are addressed in a coordinated manner in the form of a constrained optimization problem that utilizes the knowledge of the stator current evolution—as described by its gradient—within the prediction horizon. Solving this problem yields the optimal real-time modification of the offline-computed OPP which guarantees that very low—and close to its theoretical minimum value—stator current TDD is produced at steady state, and very short settling times during transients. To highlight the effectiveness of the proposed strategy, a variable speed drive system consisting of a three-level neutral point clamped (NPC) inverter and an MV induction machine serves as a case study.

**Index Terms**—Medium-voltage (MV) drives, model predictive control (MPC), optimized pulse patterns (OPPs), reference trajectory tracking, optimal control, pulse width modulation (PWM).

## I. INTRODUCTION

MARKET trends, including but not limited to industrial drive applications, electrification, renewable power generation, etc., have boosted the annual growth of medium-voltage (MV) drives. Such drives are operated at switching frequencies of a few hundred Hertz to keep the switching power losses low. In doing so, however, the stator current harmonics increase, giving rise to increased thermal losses in the machine.

To address this, optimized pulse patterns (OPPs) can be employed since they can produce very low current distortions at low switching frequencies [1]. This is due to the fact that OPPs—more specifically, the optimal switching angles over a quarter of the fundamental period—are computed in an offline procedure by minimizing an objective function that captures the stator current total demand distortion (TDD) over all possible operating points, while assuming quarter- and half-wave symmetry. As a result, the offline-computed

OPPs, when applied to a machine, produce the (theoretical) minimum current TDD for a given pulse number (i.e., switching frequency), thus ensuring the best possible steady-state behavior—as quantified by the current TDD—of the drive [2]. Due to the lack of a symmetric modulation cycle of fixed length as well as discontinuities in the switching angles with respect to the modulation index, OPPs cannot be easily utilized in a closed-loop control setting. For this reason, OPPs are typically employed by low-bandwidth controllers, such as scalar control, or low-bandwidth field oriented control (FOC), implying that the dynamic behavior of the drive is poor [3].

To utilize OPPs with a fast controller, [2]–[4] introduced the concept of stator *current* trajectory tracking, according to which the stator current space vector is forced to follow its optimal reference trajectory in a deadbeat manner. This method, however, is susceptible to parameter variations and changes in the operating conditions. As an improvement to that concept, stator *flux* trajectory control was proposed in [5] and [6], which does not depend on the machine parameters. Thus, this method shows a high degree of robustness to possible variations. Nevertheless, for this control strategy to perform well a complicated observer is required since there is no distinction between the fundamental and the ripple components of the stator current and flux linkage [5].

Despite the inherent disadvantages of the aforementioned methods, they demonstrated that by combining the control and modulation problems in one computational stage, OPPs can be effectively manipulated with a high-bandwidth controller. Given this, model predictive control (MPC), especially in its form as direct controller, is an excellent control method for OPPs. This is thanks to the fact that MPC is a multiple-input multiple-output (MIMO) control method that can simultaneously address several—and occasionally conflicting—control objectives [7]. Moreover, system constraints can be explicitly taken into account while, owing to the receding horizon policy, a high degree of robustness to parameter variations and disturbances is provided. Finally, the constrained optimization problem formulated in the framework of direct MPC accounts for both the control and modulation problems, implying that optimal steady-state and dynamic system performance are ensured [8].

To exploit the advantages of MPC and OPPs, [9] proposed an MPC-based strategy to manipulate OPPs in real time. This method was later experimentally verified in industrial MV drive systems [10], [11]. As shown, owing to the optimal na-

M. A. W. Begh and P. Karamanakos are with the Faculty of Information Technology and Communication Sciences, Tampere University, 33101 Tampere, Finland; e-mail: mirza.begh@tuni.fi, p.karamanakos@ieee.org

T. Geyer is with ABB System Drives, 5300 Turgi, Switzerland; e-mail: t.geyer@ieee.org

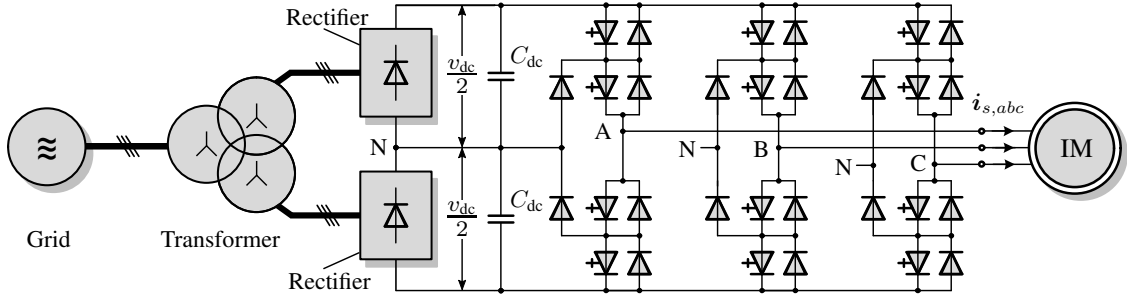


Fig. 1: Medium voltage (MV) variable speed drive (VSD) system consisting of a three-level three-phase neutral point clamped (NPC) voltage source inverter and an induction motor (IM). The inverter has a fixed neutral point potential. The dc link comprises two full-bridge rectifiers connected to the grid via a three-phase transformer.

ture of both MPC and OPPs, very low values of stator current TDD can be achieved, while the behavior of the drive during transients exhibits the typical features of direct controllers, i.e., very short settling times without over/undershoots. This method, however, is difficult to extend to more complex systems. Moreover, it is not straightforward to account for multiple control objectives.

Motivated by the observations made above, this paper proposes an alternative MPC strategy to control the stator currents—and thus the electromagnetic torque and magnetization—of an MV machine by manipulating OPPs in real time. To do so, similar to [12], the gradients of the controlled variables, i.e., the stator currents, are utilized so that their evolutions can be predicted in a simple, yet accurate manner. With this information, a constrained optimization problem is formulated and solved in real time that computes the optimal required modifications of OPPs. As a result, superior steady-state performance is achieved thanks to the inherent characteristics of OPPs, while the *direct* and *optimal* manipulation of their switching time instants by the proposed controller—named gradient-based predictive pulse pattern control (GP<sup>3</sup>C)—allows for very fast transients.

To highlight the potential benefits of the proposed method, an MV drive system consisting of a three-level neutral point clamped (NPC) voltage source inverter and an induction machine (IM) is considered. Our results in this work, along with those in the analysis part [13],<sup>1</sup> show that the proposed control scheme provides significant performance benefits compared to conventional control methods such as FOC with carrier-based pulse width modulation (CB-PWM) or space vector modulation (SVM).

In summary, the contributions of this paper are three-fold. First, a highly versatile modeling approach, namely, the gradients of the controlled variables, is adopted, which allows for a simple formulation of the optimization problem underlying MPC for MV drives. This flexibility also enables the straightforward adaptation of the method to other case studies. Second, the combination of MPC—formulated as current trajectory tracking controller—and OPPs ensures an excellent steady-state performance and superior dynamic be-

havior due to the optimal real-time modification of the OPPs, as demonstrated with the presented results as well as those in its analysis part [13]. Third, the proposed control method can effectively deal with system non-idealities, such as persistent harmonics due to a significant dc-link voltage ripple, owing to the employed receding horizon policy.

The remainder of the paper is organized as follows. Section II describes the model of the MV drive system case study used throughout the two papers. Section III summarizes the basic characteristics of OPPs and discusses the computation of the stator current reference trajectory which is subsequently used by the MPC algorithm. The proposed GP<sup>3</sup>C scheme is presented in detail in Section IV, along with the formulation of the optimal control problem as a quadratic program (QP). Section V assesses the performance of the proposed control strategy during steady-state and transient operating conditions and compares it with that of FOC with SVM. Finally, conclusions are drawn in Section VI.

## II. PHYSICAL MODEL OF THE SYSTEM

In this section the mathematical model of the system under consideration is derived in the stationary orthogonal  $\alpha\beta$ -frame. For this reason, any variable  $\xi_{abc} = [\xi_a \ \xi_b \ \xi_c]^T$  in the three-phase  $abc$ -plane is transformed to  $\xi_{\alpha\beta} = [\xi_\alpha \ \xi_\beta]^T$  in the stationary orthogonal  $\alpha\beta$ -plane through  $\xi_{\alpha\beta} = \mathbf{K}\xi_{abc}$  with the transformation matrix<sup>2</sup>

$$\mathbf{K} = \frac{2}{3} \begin{bmatrix} 1 & -\frac{1}{2} & -\frac{1}{2} \\ 0 & \frac{\sqrt{3}}{2} & -\frac{\sqrt{3}}{2} \end{bmatrix}. \quad (1)$$

Note that in this paper all quantities are normalized and presented in the per unit (p.u.) system.

### A. Model of the Inverter

Consider the MV drive system consisting of a three-level NPC voltage source inverter and an IM as shown in Fig. 1. The dc link of the inverter is supplied by two full-bridge diode rectifiers. These are connected to a symmetrical three-phase grid via a Y-YY transformer.<sup>3</sup> The dc-link voltage has an

<sup>2</sup>Throughout the paper, variables in the  $abc$ -plane are denoted by their corresponding subscript. For those in the  $\alpha\beta$ -plane the subscript is omitted to simplify the notation.

<sup>3</sup>Unlike the standard Y-Y $\Delta$  configuration, a Y-YY configuration is chosen in this work to increase the dc-link voltage ripple. This forces the controller to operate in a more adverse situation, enabling the verification of its performance in a somewhat extreme test scenario.

<sup>1</sup>The current paper and the performance analysis part [13] are a two-part series, where the first part, i.e., the present paper, is dedicated to the control algorithm formulation and analysis as well as some key results that highlight the performance improvements achieved with GP<sup>3</sup>C. The second part presents a detailed performance analysis based on a real-time hardware-in-the-loop system along with the relevant implementation aspects.

instantaneous (i.e., non-constant) value  $v_{dc}$  with the average value  $V_{dc}$ . Moreover, the neutral point (N) potential is assumed to be fixed and equal to zero.

The switch position in phase  $x \in \{a, b, c\}$  of the inverter can be modeled by the integer variable  $u_x \in \mathcal{U} = \{-1, 0, 1\}$ . Depending on the *single-phase* switch position  $u_x$ , the output voltage of each phase can assume one of the discrete voltage levels  $-v_{dc}/2$ , 0, and  $v_{dc}/2$ . By aggregating the single-phase switch positions  $u_x$  to the *three-phase* switch position  $\mathbf{u}_{abc} = [u_a \ u_b \ u_c]^T \in \mathcal{U}^3$ , the output voltage of the inverter, which is equal to the stator voltage  $\mathbf{v}_s$ , is

$$\mathbf{v}_s = \frac{v_{dc}}{2} \mathbf{u} = \frac{v_{dc}}{2} \mathbf{K} \mathbf{u}_{abc}. \quad (2)$$

### B. Model of the Induction Machine

The IM considered in this work has a squirrel-cage rotor. Its dynamics are represented in terms of the stator current  $\mathbf{i}_s$ , the rotor flux  $\psi_r$ , and the rotor angular speed  $\omega_r$ . The machine parameters are the stator and rotor resistance,  $R_s$  and  $R_r$ , respectively, the stator leakage, rotor leakage, and mutual reactance,  $X_{ls}$ ,  $X_{lr}$ , and  $X_m$ , respectively.<sup>4</sup> Introducing the moment of inertia  $H$  and the mechanical load torque  $T_\ell$ , the following set of differential equations describe the dynamics of the IM, see [14] and [15]

$$\frac{d\mathbf{i}_s}{dt} = -\frac{1}{\tau_s} \mathbf{i}_s + \left( \frac{1}{\tau_r} \mathbf{I}_2 - \omega_r \begin{bmatrix} 0 & -1 \\ 1 & 0 \end{bmatrix} \right) \frac{X_m}{D} \psi_r + \frac{X_r}{D} \mathbf{v}_s \quad (3a)$$

$$\frac{d\psi_r}{dt} = \frac{X_m}{\tau_r} \mathbf{i}_s - \frac{1}{\tau_r} \psi_r + \omega_r \begin{bmatrix} 0 & -1 \\ 1 & 0 \end{bmatrix} \psi_r \quad (3b)$$

$$\frac{d\omega_r}{dt} = \frac{1}{H} (T_e - T_\ell), \quad (3c)$$

where  $\tau_s = X_r D / (R_s X_r^2 + R_r X_m^2)$  is the transient stator time constant, and  $\tau_r = X_r / R_r$  is the time constant of the rotor winding. Moreover, the constant  $D$  is defined as  $D = X_s X_r - X_m^2$ , with  $X_s = X_{ls} + X_m$  and  $X_r = X_{lr} + X_m$  being the stator and rotor self-reactance, respectively. Moreover,  $\mathbf{I}_2$  is a two-dimensional identity matrix. Finally, the electromagnetic torque  $T_e$  is given by

$$T_e = \frac{X_m}{X_r} (\psi_r \times \mathbf{i}_s) = \frac{X_m}{X_r} (\psi_{r\alpha} i_{s\beta} - \psi_{r\beta} i_{s\alpha}). \quad (4)$$

### C. State-Space Model

By considering as input to the drive system the three-phase switch position  $\mathbf{u}_{abc}$ , as output the stator current, i.e.,  $\mathbf{y} = [i_{s\alpha} \ i_{s\beta}]^T \in \mathbb{R}^2$ , and by choosing as state variables the stator current and rotor flux,<sup>5</sup> i.e., the state vector is  $\mathbf{x} = [i_{s\alpha} \ i_{s\beta} \ \psi_{r\alpha} \ \psi_{r\beta}]^T \in \mathbb{R}^4$ , the continuous-time state-space model can be written with the help of (2) and (3) as

$$\frac{d\mathbf{x}(t)}{dt} = \mathbf{F} \mathbf{x}(t) + \mathbf{G} \mathbf{u}_{abc}(t) \quad (5a)$$

$$\mathbf{y}(t) = \mathbf{C} \mathbf{x}(t), \quad (5b)$$

<sup>4</sup>All rotor quantities are referred to the stator circuit.

<sup>5</sup>Note that  $\omega_r$  changes slowly compared with  $\mathbf{i}_s$  and  $\psi_r$ . For this reason, in the subsequent model derivation, it is considered as a (slowly) varying parameter instead of a state variable.

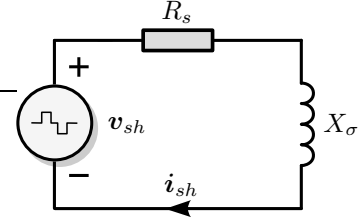


Fig. 2: Harmonic model of an induction machine.

where the system  $\mathbf{F} \in \mathbb{R}^{4 \times 4}$ , input  $\mathbf{G} \in \mathbb{R}^{4 \times 3}$ , and output  $\mathbf{C} \in \mathbb{R}^{2 \times 4}$  matrices are provided in Appendix A.

### D. Harmonic Model of the Machine

The induction machine model (3) describes the machine behavior during both steady-state and dynamic operation. This model, however, contains information for both the fundamental component of the quantities of interest (e.g., stator current, stator voltage, and rotor flux) as well as their harmonics. When the focus is solely on the harmonics, then the harmonic model of the machine shown in Fig. 2 is preferred since it can clearly evaluate the impact of the voltage harmonics on the machine. As shown in [7, Section 2.2], the voltage equation of this model is given by

$$\mathbf{v}_{sh} = R_s \mathbf{i}_{sh} + X_\sigma \frac{d\mathbf{i}_{sh}}{dt}, \quad (6)$$

where  $\mathbf{v}_{sh}$  and  $\mathbf{i}_{sh}$  is the harmonic voltage and current, respectively, while  $X_\sigma = D/X_r$  is the total leakage reactance of the machine.

## III. OPTIMIZED PULSE PATTERNS

This section presents the key properties of OPPs. Furthermore, the optimal steady-state stator current reference trajectory is derived. Finally, the challenges that relate to the closed-loop control of OPPs are summarized.

### A. Key Properties of OPPs

OPP is computed offline for a given modulation index  $m$  by minimizing an objective function which typically accounts for the load (e.g., stator) current distortion, as quantified by its TDD [1]. Moreover, to ensure that the only harmonics with non-zero amplitude are those at odd multiples of the fundamental frequency, quarter- and half-wave symmetry is imposed on the OPP, even though symmetry relaxations may achieve lower current TDDs, as recently shown in [16]. This optimization procedure takes place for the whole range of modulation indices  $m \in [0, 4/\pi]$  as well as a wide range of single-phase switching transitions that occur over one quarter of the fundamental period, i.e.,  $d = 1, 2, \dots \in \mathbb{N}^+$ . Note that for a three-level converter, the number of switching transitions  $d$  is equal to the pulse number. The latter is defined as the ratio between the (device) switching frequency and the fundamental frequency. Since  $d$  is an integer, synchronization of the OPP with the fundamental voltage waveform is implied, meaning that no interharmonics exist.<sup>6</sup>

<sup>6</sup>Therefore, modulation based on OPPs is a so-called synchronous PWM method.

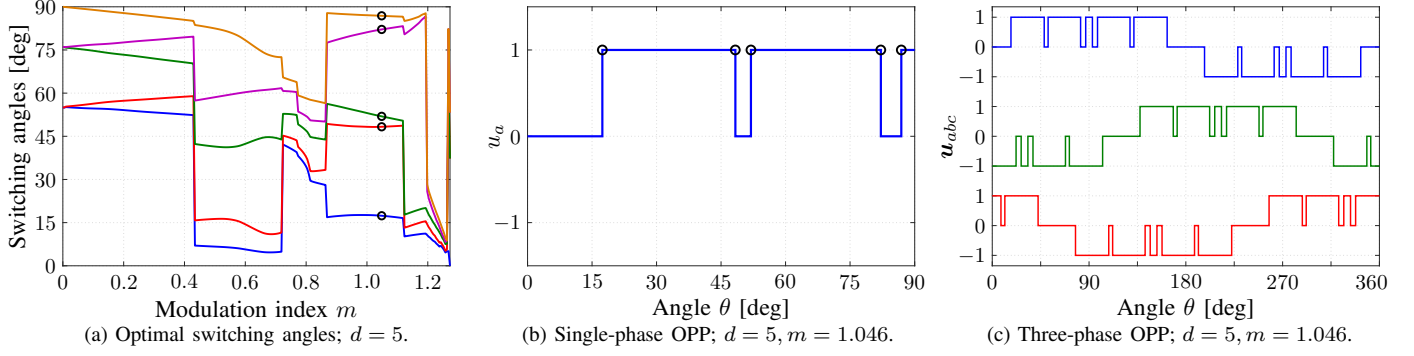


Fig. 3: Optimized pulse pattern (OPP)  $p(d, m)$  for a three-level converter with  $d = 5$  switching angles per quarter of the fundamental period. The single- and three-phase pulse patterns correspond to the modulation index  $m = 1.046$ . The optimal switching angles for  $m = 1.046$  are indicated by (black) circles.

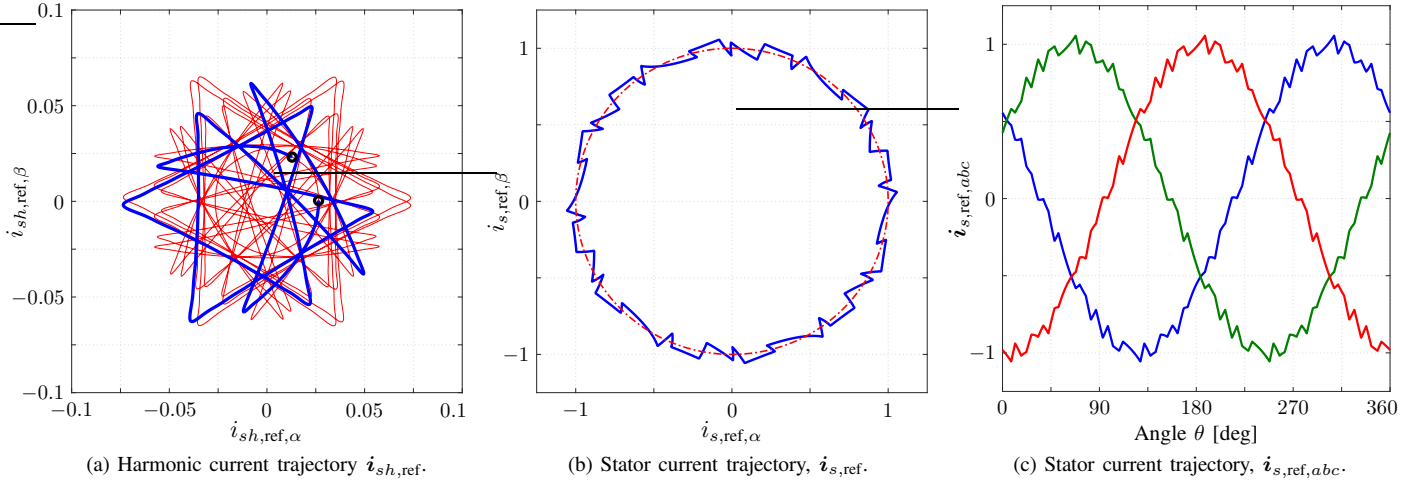


Fig. 4: Current reference trajectory for the OPP shown in Fig. 3. The blue line in (a) highlights  $\dot{i}_{sh,ref}$  for one-sixth of the fundamental period. The red (dash-dotted) line in (b) is the fundamental component  $\dot{i}_{s1,ref}$  of the stator current.

By following this optimization procedure a set of switching angles  $\alpha \in [0, 90^\circ]^d$  is computed as a function of  $m$  and  $d$ , as visualized in Fig. 3(a) for  $d = 5$ . Hence, a single-phase OPP  $u(\theta)$  can be represented as a function  $p(d, m)$ , the output of which is the set of  $d$  switching angles  $\alpha$ . To exemplify this, Fig. 3(b) illustrates a single-phase three-level OPP for  $d = 5$  and  $m = 1.046$  (i.e., the OPP  $p(5, 1.046)$ ) over a quarter of a period. Moreover, Fig. 3(c) shows the corresponding three-phase OPP  $u_{abc}(\theta)$ . To generate the latter, basic symmetry properties of the single-phase OPP are exploited, while a balanced three-phase system is assumed. Specifically, the quarter- and half-wave symmetry characteristics of the single-phase OPP are used to calculate the OPP over the fundamental period, while the pulse patterns of the two remaining phases are generated based on the phase difference of the three phases, i.e., a shift by  $120^\circ$  and  $240^\circ$  occurs for phases  $b$  and  $c$ , respectively. A detailed explanation of OPP calculation for multilevel inverters can be found in [17].

Based on the procedure and OPP characteristics described above, it can be understood that the offline-computed OPPs generate the theoretical minimum current TDD when applied to an IM. In doing so, minimal iron and copper losses, and thus thermal losses, can be achieved. For this reason, OPPs are the most promising modulation method when operation at

very low switching frequencies is required [7], [17].

### B. Optimal Steady-State Stator Current Trajectory

As explained earlier, the stator current generated by the nominal OPP exhibits the lowest possible harmonic distortions. Therefore, to achieve the best possible steady-state performance—in terms of current TDD—the actual stator current of the machine should be as close as possible to the nominal OPP-generated current trajectory. This implies that the optimal steady-state stator current can be used as a reference trajectory in a closed-loop setting.

To compute the optimal steady-state current  $\dot{i}_{s,ref}$  its components need to be analyzed. Given that  $\dot{i}_{s,ref}$  is a superposition of the fundamental  $\dot{i}_{s1,ref}$  and harmonic  $\dot{i}_{sh,ref}$  components, i.e.,

$$\dot{i}_{s,ref} = \dot{i}_{s1,ref} + \dot{i}_{sh,ref}, \quad (7)$$

the components  $\dot{i}_{s1,ref}$  and  $\dot{i}_{sh,ref}$  need to be derived. The former can be produced by an outer control loop which controls the degree of machine magnetization and electromagnetic torque. As for the harmonic component  $\dot{i}_{sh,ref}$ , it can be computed based on the harmonic model of the IM (see Fig. 2) and the nominal OPP  $u_{abc}(\theta)$  of interest. More specifically, by performing harmonic analysis of the OPP  $u_{abc}(\theta)$ , the

amplitude  $\hat{u}_n$  and phase  $\hat{\phi}_n$  of the  $n^{\text{th}}$  voltage harmonic, where  $n = 2\kappa + 1$ ,  $\kappa \in \mathbb{N}^+$ , can be found. Given (6), and assuming  $R_s \approx 0$ —as is the case with MV machines—and a stiff dc-link voltage  $V_{\text{dc}}$ , the  $n^{\text{th}}$  harmonic of the current is [7, Section 3.4]

$$\hat{i}_{s,n} = \frac{V_{\text{dc}}}{2X_\sigma} \frac{\hat{u}_n}{n\omega_1}, \quad (8)$$

with  $\omega_1 = 2\pi f_1$  being the fundamental angular frequency. Hence, with the knowledge of the amplitude  $\hat{i}_{s,n}$  and phase  $\hat{\phi}_n$  of the current harmonics,  $\hat{i}_{sh,\text{ref}}$  is derived in an offline procedure according to the following expression

$$\hat{i}_{sh,\text{ref}}(\theta) = \sum_{n=5,7,\dots,N_h} \hat{i}_{sn} \sin(n\theta - \hat{\phi}_n), \quad (9)$$

where  $N_h$  is the maximum harmonic order to be included in the current reference. It is important to stress that in (9) the non-zero harmonics are located at non-triplen, odd multiples of the fundamental frequency, since the triplen voltage harmonics ( $n = 3, 9, 15, \dots$ ) are in phase, i.e., they are common-mode harmonics which do not drive a harmonic current. Moreover, due to symmetries that apply to the single- and three-phase OPP, the resulting harmonic current repeats itself every  $60^\circ$ . For this reason, only one-sixth of the fundamental period needs to be computed and stored in a look-up-table (LUT) for later use, which greatly reduces the required memory resources. To ensure operation over the whole range of operating points and relevant switching frequencies, the above procedure is repeated for various numbers of switching angles  $d$  and modulation indices  $m$ .

The construction of the complete optimal steady-state current trajectory is done in real time when required by the controller. To this aim, the harmonic current of the first  $60^\circ$  sector is rotated by  $(\zeta - 1) \cdot 60^\circ$  for the remaining five  $60^\circ$  sectors ( $\zeta = 2, 3, \dots, 6$ ). This is visualized in Fig. 4(a), where the harmonic current generated by the OPP in Fig. 3 is shown. Therein, a  $60^\circ$  sector is highlighted to elucidate the aforementioned procedure, while the initial and final values of this section are marked as black empty circles. The complete optimal (i.e., reference) steady-state trajectory in the  $\alpha\beta$ -plane is shown in Fig. 4(b). As can be seen, combining the fundamental component  $\hat{i}_{s1,\text{ref}}$  (dash-dotted line) with the optimal current ripple  $\hat{i}_{sh,\text{ref}}$  (see Fig. 4(a)), gives rise to the optimal current trajectory  $\hat{i}_{s,\text{ref}}$  (solid line in Fig. 4(b)). Finally, for reasons of completeness, Fig. 4(c) shows the optimal current trajectory in the  $abc$ -plane.

### C. OPPs in a Closed-Loop Control Setting

As can be observed in Fig. 3(c), OPPs—as opposed to conventional modulation methods, such as CB-PWM or SVM—do not exhibit a symmetric modulation cycle. This implies that when sampling occurs, not only the fundamental component of the current is sampled—as is the case with synchronous SVM or CB-PWM—but also its ripple. This is clearly illustrated in Fig. 4(a), where, as shown, the ripple of the current is never zero. This means that linear controllers, such as proportional-integral (PI) controllers, cannot be employed to manipulate OPPs since they will interpret the ripple current as a steady-state error, thus they will try to remove it. In doing so, however,

the controller will unnecessarily modify the nominal OPP, deteriorating its harmonic performance. To address this issue, it is common practice to use OPPs with a low-bandwidth controller.

Another reason that hinders the utilization of OPPs with a high-bandwidth controller is the existence of discontinuities in the nominal OPP switching angles. As can be observed in Fig. 3(a), the switching angles change, in general, smoothly with the modulation index  $m$ , but for some values of  $m$ , they change abruptly, e.g., for  $m = 0.43, 0.72, 0.87, 1.12$  and  $1.2$  when  $d = 5$ . This implies that when operation within the neighborhood of these modulation indices is required, significant current excursions may occur when crossing a discontinuity. To avoid this, a controller that can quickly modify the OPP is required. However, as explained above, linear controllers need to be tuned such that they act in a very slow manner, rendering them unsuitable for fast closed-loop control. Hence, a trajectory-based control technique needs to be devised that combines control and modulation in one computational stage. This is the subject of the following section.

## IV. GRADIENT-BASED PREDICTIVE PULSE PATTERN CONTROL ALGORITHM

To address the control problem of the MV induction machine fed by a three-level NPC inverter, we propose a control approach based on the combination of OPPs [1], [18] and gradient-based direct MPC [12], [19]. As a result, the inherent characteristics of both adopted methods are fully exploited. More specifically, thanks to the OPPs, excellent steady-state performance is achieved as quantified by the very low current TDD, which is as close to its theoretical minimum value as possible. Moreover, direct MPC manages to manipulate the OPPs in real time in an optimal and effective manner, thus achieving fast dynamic control with short settling times. In the sequel of this section, the main principle and characteristics of the proposed control algorithm are presented.

### A. Control Problem

The main control objectives of the controller are two. First, the proposed control approach should aim for accurate regulation of the stator current along its optimal current reference trajectory (see Section III-B), so that the resulting current has the lowest possible harmonic distortions. Second, the controller should have high bandwidth to achieve fast rejection of disturbances and as fast current and torque response times as possible.

To meet the above-mentioned control goals, the offline-computed nominal OPP is used as a baseline pattern and modified in real time to achieve closed-loop current control, operating in the discrete time domain with the sampling interval  $T_s$  and the time step  $k \in \mathbb{N}$ . The required pattern modifications are computed in an optimal manner by solving a constrained optimization problem with receding horizon. Hence, the MPC algorithm modifies the nominal OPP *locally*, within a time window  $T_p = N_p T_s$ , where  $N_p$  is the number

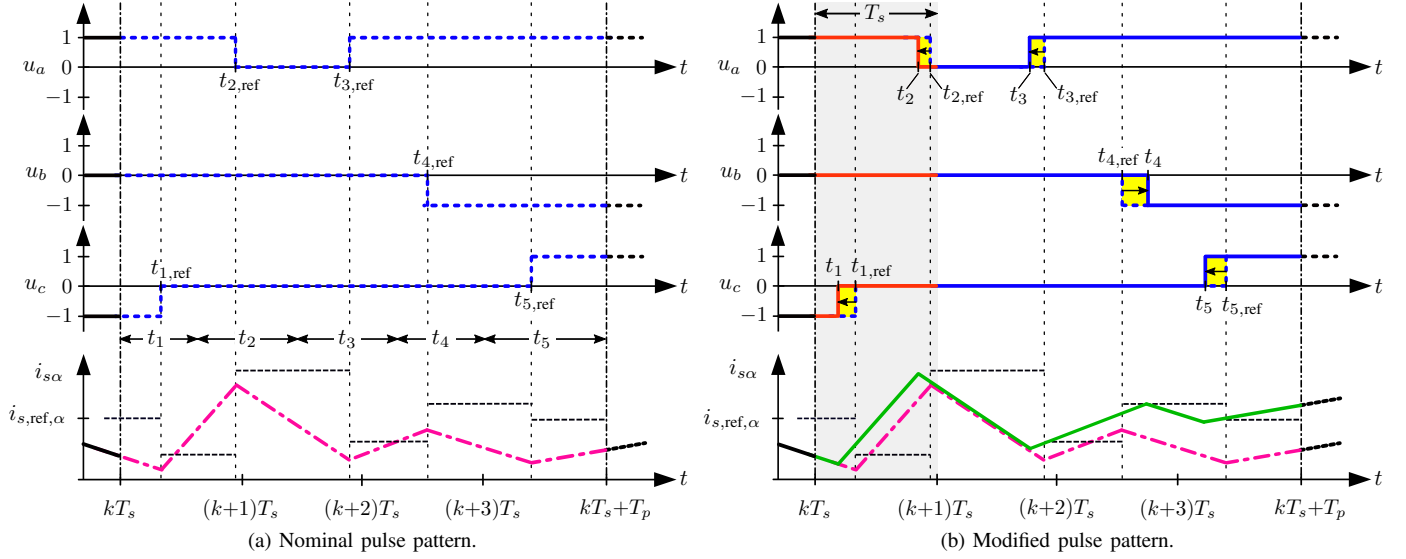


Fig. 5: Three-phase three-level OPP with nominal switching instants  $t_{i,\text{ref}}$  and the modified switching instants  $t_i$ , where five switching instants, i.e.,  $i \in \{1, 2, \dots, 5\}$ , fall within a four-step ( $T_p = 4T_s$ ) prediction horizon. (a) Nominal (to-be-modified) OPP and the lower and upper bounds on the switching instants (indicated with arrows). (b) Modified pulse pattern based on the shifted switching instants as computed by GP<sup>3</sup>C. The bottom figures show the evolution of the stator current  $i_{s\alpha}$  within the prediction horizon. The dash-dotted (magenta) line shows the (linearized) current trajectory when applying the nominal OPP, while the solid (green) line depicts the (linearized) current trajectory based on the modified pulse pattern. The dashed (black) line is the current reference  $i_{s,\text{ref},\alpha}$ , sampled at the nominal OPP time instants.

of time steps. Beyond this window steady-state operation is assumed while applying the nominal OPP.

Given the above, the following vectors are introduced:

$$\mathbf{t}_{\text{ref}} = [t_{1,\text{ref}} \ t_{2,\text{ref}} \ \dots \ t_{z,\text{ref}}]^T, \quad (10a)$$

$$\mathbf{U} = [\mathbf{u}_{abc}^T(t_0) \ \mathbf{u}_{abc}^T(t_{1,\text{ref}}) \ \dots \ \mathbf{u}_{abc}^T(t_{z,\text{ref}})]^T, \quad (10b)$$

$$\mathbf{t} = [t_1 \ t_2 \ \dots \ t_z]^T, \quad (10c)$$

where  $\mathbf{t}_{\text{ref}} \in \mathbb{R}^z$  is the vector of the  $z \in \mathbb{N}$  switching time instants (which correspond to the switching angles  $\alpha$ ) of the nominal OPP within  $T_p$ . Moreover,  $\mathbf{U} \in \mathcal{U}^{3(z+1)}$  is the vector of the corresponding OPP switch positions,<sup>7</sup> and  $\mathbf{t} \in \mathbb{R}^z$  includes the modified switching time instants that need to be computed in real time. Finally, it is worth mentioning that the OPP switching instants  $\mathbf{t}_{\text{ref}}$  divide the prediction horizon  $T_p$  into smaller subintervals, i.e.,  $[0, t_{1,\text{ref}})$ ,  $[t_{1,\text{ref}}, t_{2,\text{ref}})$ ,  $\dots$ ,  $[t_{z,\text{ref}}, T_p)$ .

**Example 1:** Consider the nominal OPP shown as the dashed (blue) line in Fig. 5(a). For the illustrated OPP, the initial switch position at  $t_0 \equiv kT_s$  is the one applied at the end of the previous sampling interval, i.e.,  $\mathbf{u}_{abc}(t_0) = \mathbf{u}_{abc}(t_0^-) = [1 \ 0 \ -1]^T$ . As can be seen, five nominal switching time instants  $t_{1,\text{ref}}$ ,  $t_{2,\text{ref}}$ ,  $t_{3,\text{ref}}$ ,  $t_{4,\text{ref}}$  and  $t_{5,\text{ref}}$  fall within the prediction horizon  $T_p$ , and the corresponding switch positions are  $\mathbf{u}_{abc}(t_{1,\text{ref}})$ ,  $\mathbf{u}_{abc}(t_{2,\text{ref}})$ ,  $\mathbf{u}_{abc}(t_{3,\text{ref}})$ ,  $\mathbf{u}_{abc}(t_{4,\text{ref}})$  and  $\mathbf{u}_{abc}(t_{5,\text{ref}})$ . The controller should locally re-optimize the nominal OPP within  $T_p$  by modifying the nominal OPP time instants, i.e., by computing the switching time instants  $t_1$ ,  $t_2$ ,  $t_3$ ,  $t_4$  and  $t_5$  (see Fig. 5(b)), such that the desired control objectives are met. ■

<sup>7</sup>It should be noted that the first entry of  $\mathbf{U}$  is the switch position applied last in the previous sampling interval, i.e.,  $\mathbf{u}_{abc}(t_0) \equiv \mathbf{u}_{abc}(t_0^-)$ .

## B. Control Method

Considering that the MPC scheme is designed as a current controller, the minimum current TDD results when perfect tracking of the optimal current reference trajectory is achieved. To this aim, the objective function captures the (squared) rms error of the stator current within the prediction horizon  $T_p$ , while minimizing the changes in the nominal OPP to avoid unnecessary modifications that can detract from the steady-state performance of the controller. Hence, the proposed objective function is

$$J = \frac{1}{T_p} \left( \int_0^{T_p} \|\mathbf{i}_{s,\text{ref}}(t) - \mathbf{i}_s(t)\|_2^2 dt \right) + \lambda_t \|\Delta \mathbf{t}\|_2^2, \quad (11)$$

where  $\Delta \mathbf{t} = \mathbf{t}_{\text{ref}} - \mathbf{t}$  are the (to-be-applied) modifications on the nominal OPP. The weighting factor  $\lambda_t \geq 0$  penalizes the modifications  $\Delta \mathbf{t}$  and provides the controller designer with a degree of freedom; by appropriately tuning it the first term of function (11) can be prioritized over the second one, or vice versa.

Since the first term in function (11) accounts for the (squared) rms current error, it is a cubic function of time [12], [19]. As a result, the associated optimization problem is nonconvex, which is not trivial to solve. To avoid this pitfall, a simplification is introduced to turn the optimization problem into a convex one, thus greatly speeding up the solution process [20]. Specifically, the current tracking error is penalized only at the finite number of OPP switching time instants. Consequently, the objective function (11) takes the form

$$J = \sum_{i=1}^z \left( \|\mathbf{i}_{s,\text{ref}}(t_{i,\text{ref}}) - \mathbf{i}_s(t_i)\|_2^2 \right) + \lambda_t \|\Delta \mathbf{t}\|_2^2, \quad (12)$$

which is now a quadratic (i.e., convex) function of time.

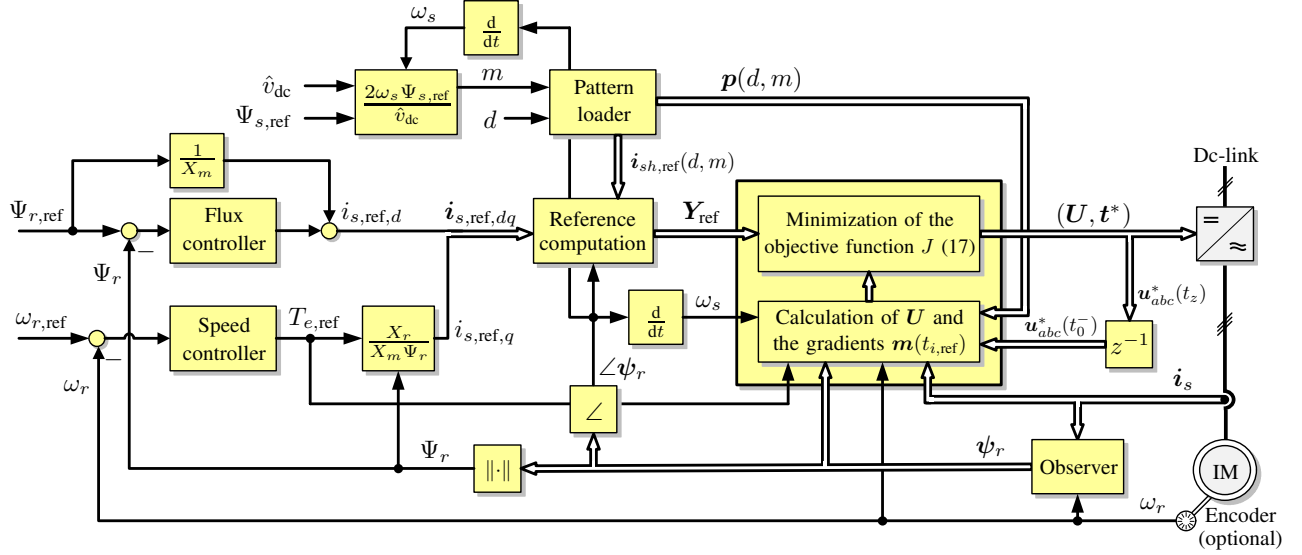


Fig. 6: Block diagram of the gradient-based predictive pulse pattern control (GP<sup>3</sup>C) scheme.

Note that on the basis that the prediction horizon  $T_p$  is long enough such that as many switching time instants as possible are included, the first term in (12) accounts in a coarse, yet sufficiently accurate, manner for the rms current error.<sup>8</sup>

According to (12), in order to compute the modified switching time instants  $t$ , the evolution of the stator current  $i_s$  within the horizon is required. With this, the difference between the predicted current and the (sampled) optimal current reference can be computed. Since the prediction horizon  $T_p$  is much shorter than the fundamental period  $T_1$ , i.e.,  $T_p \ll T_1$ , this task can be simplified by considering the evolution of the current within each subinterval  $\Delta t_{\ell,\text{ref}}$ , where

$$\Delta t_{\ell,\text{ref}} = t_{\ell+1,\text{ref}} - t_{\ell,\text{ref}}, \quad (13)$$

and  $\ell \in \{0, 1, 2, \dots, z-1\}$ , with  $t_{0,\text{ref}} = t_0$ . Given the measured or estimated state at  $t_0$ ,  $\mathbf{x}(t_0)$ , as well as the fact that the OPP switch positions  $\mathbf{u}_{abc}$  within  $T_p$  are known (see (10b)), the state at the nominal OPP switching instants  $t_{i,\text{ref}}$  can be found. Specifically, to compute  $\mathbf{x}(t_{1,\text{ref}})$ ,  $\mathbf{x}(t_{2,\text{ref}})$ ,  $\dots$ ,  $\mathbf{x}(t_{z,\text{ref}})$ , the state is predicted in a consecutive manner based on the following discrete-time state-space model,

$$\mathbf{x}(t_{\ell+1,\text{ref}}) = \mathbf{A}\mathbf{x}(t_{\ell,\text{ref}}) + \mathbf{B}\mathbf{u}_{abc}(t_{\ell,\text{ref}}) \quad (14a)$$

$$\mathbf{y}(t_{\ell,\text{ref}}) = \mathbf{C}\mathbf{x}(t_{\ell,\text{ref}}), \quad (14b)$$

where the discrete-time matrices  $\mathbf{A}$  and  $\mathbf{B}$  are computed from the continuous-time model (5) by employing exact discretization, i.e.,  $\mathbf{A} = \mathbf{e}^{\mathbf{F}\Delta t_{\ell,\text{ref}}}$  and  $\mathbf{B} = -\mathbf{F}^{-1}(\mathbf{I}_4 - \mathbf{A})\mathbf{G}$ , where  $\mathbf{e}$  is the matrix exponential. Note that for an accurate computation of  $\mathbf{x}(t_{\ell,\text{ref}})$ , the continuous-time matrices  $\mathbf{F}$  and  $\mathbf{G}$  are discretized within each subinterval based on the respective subinterval length  $\Delta t_{\ell,\text{ref}}$ .

With the knowledge of  $\mathbf{x}(t_{\ell,\text{ref}})$ , the stator current trajectories within each subinterval  $\Delta t_{\ell,\text{ref}}$  can be described by their

corresponding gradients, i.e.,

$$\mathbf{m}(t_{\ell,\text{ref}}) = \frac{\mathbf{y}(t_{\ell+1,\text{ref}}) - \mathbf{y}(t_{\ell,\text{ref}})}{\Delta t_{\ell,\text{ref}}} = \mathbf{C} \frac{\mathbf{x}(t_{\ell+1,\text{ref}}) - \mathbf{x}(t_{\ell,\text{ref}})}{\Delta t_{\ell,\text{ref}}}. \quad (15)$$

To better understand the above concept, the following example is provided.

**Example 2:** Consider the nominal OPP in Fig. 5(a) with five switching instants within the horizon, i.e.,  $z = 5$ . These instants divide the prediction horizon into six subintervals. Within each subinterval, it is assumed that the stator current evolves with a constant gradient, as exemplified in Fig. 5 for the  $\alpha$ -component of the stator current  $i_{s\alpha}$  (see the dash-dotted, magenta line). To compute this evolution, as described by the associated gradients, we begin with the first subinterval  $[t_0, t_{1,\text{ref}})$ . In a first step, matrices  $\mathbf{F}$  and  $\mathbf{G}$  are discretized based on  $\Delta t_{0,\text{ref}} = t_{1,\text{ref}} - t_0$ . With this information, the state at the end of the subinterval  $\mathbf{x}(t_{1,\text{ref}})$  is predicted based on (14), and by using the measured or estimated state  $\mathbf{x}(t_0)$  and the initial switch position of the OPP  $\mathbf{u}_{abc}(t_0)$ . Following, the gradient of the stator current within this subinterval  $\mathbf{m}(t_0)$  is computed according to (15). For the second subinterval  $[t_{1,\text{ref}}, t_{2,\text{ref}})$ , matrices  $\mathbf{F}$  and  $\mathbf{G}$  are discretized based on  $\Delta t_{1,\text{ref}} = t_{2,\text{ref}} - t_{1,\text{ref}}$ . The state at  $t_{2,\text{ref}}$ , i.e.,  $\mathbf{x}(t_{2,\text{ref}})$ , is predicted using the previously computed state  $\mathbf{x}(t_{1,\text{ref}})$  and the OPP switch position  $\mathbf{u}_{abc}(t_{1,\text{ref}})$ . Finally, the corresponding gradient of the stator current  $\mathbf{m}(t_{1,\text{ref}})$  is computed with (15). The same procedure is repeated for all the subintervals within the prediction horizon until all  $z$  gradients have been computed. ■

With the gradients  $\mathbf{m}(t_{\ell,\text{ref}})$  (see (15)), the stator current at the to-be-computed modified time instants  $t$  becomes

$$\begin{aligned} i_s(t_1) &= i_s(t_0) + \mathbf{m}(t_{0,\text{ref}})(t_1 - t_0) \\ i_s(t_2) &= i_s(t_1) + \mathbf{m}(t_{1,\text{ref}})(t_2 - t_1) \\ &\vdots \\ i_s(t_z) &= i_s(t_{z-1}) + \mathbf{m}(t_{z-1,\text{ref}})(t_z - t_{z-1}). \end{aligned} \quad (16)$$

<sup>8</sup>The approximation of the rms error by the first term in (12) is explained in more detail in Appendix B.

---

**Algorithm 1:** Gradient-based predictive pulse pattern control
 

---

Given  $\mathbf{u}_{abc}(t_0)$ ,  $\mathbf{x}(t_0)$ ,  $\mathbf{i}_{s,\text{ref},dq}$  and  $\mathbf{p}(d, m)$

0. Extract the  $z$  switching time instants and switch positions that fall within  $T_p$  from the nominal OPP  $\mathbf{p}(d, m)$  to formulate  $\mathbf{t}_{\text{ref}}$  and  $\mathbf{U}$ .
  1. Compute the current reference values  $\mathbf{i}_{s,\text{ref}}(t_{i,\text{ref}})$ ,  $i \in \{1, 2, \dots, z\}$ .
  2. Formulate the gradients  $\mathbf{m}(t_{\ell,\text{ref}})$ ,  $\ell \in \{0, 1, 2, \dots, z-1\}$ .
  3. Solve the optimization problem (21). This yields  $\mathbf{t}^*$ .
- Return  $\mathbf{t}^*(k)$  that fall within  $T_s$  and modify the OPP accordingly.
- 

Note that (16) indicates a linear prediction model that is based on nonlinear predicted samples. By using (16), and after some algebraic manipulations,<sup>9</sup> function (12) can be written in the compact form

$$J = \|\mathbf{r} - \mathbf{M}\mathbf{t}\|_2^2 + \lambda_t \|\Delta\mathbf{t}\|_2^2. \quad (17)$$

The entries of vector  $\mathbf{r} \in \mathbb{R}^{2z}$  depend on the reference values and measurements of the stator current, while those of matrix  $\mathbf{M} \in \mathbb{R}^{2z \times z}$  depend on the gradients with which the stator current evolves within the prediction horizon, see Appendix C. Finally, it should be mentioned that both  $\mathbf{r}$  and  $\mathbf{M}$  are time-varying, and their dimensions change depending on the number of OPP switching instants  $z$  that fall within the prediction horizon  $T_p$ .

### C. Control Algorithm

In this section the steps that constitute the proposed optimal control algorithm are presented. The controller is designed in the discrete-time domain, and is executed at the equally spaced discrete time instants  $kT_s$ . The outer control loop is designed in the  $dq$ -reference plane which rotates with the stator angular speed  $\omega_s$ , while the inner, current control loop is designed in the stationary orthogonal  $(\alpha\beta)$  plane. The block diagram of the proposed GP<sup>3</sup>C algorithm—including both the outer and inner loops—is presented in Fig. 6, and the pseudocode is summarized in Algorithm 1.

**Step 0.** In a preprocessing step, the modulation index  $m$  is computed. Neglecting the stator resistance, the modulation index is equal to

$$m = \frac{2}{\hat{v}_{\text{dc}}} \omega_s \Psi_{s,\text{ref}}, \quad (18)$$

where  $\hat{v}_{\text{dc}}$  is low-pass-filtered dc-link voltage and  $\Psi_{s,\text{ref}}$  the amplitude of the reference stator flux, which is typically equal to 1 p.u. so that the machine is fully magnetized. Since the voltage drop in the stator resistance is neglected in (18), the value of  $m$  corresponds to the amplitude of the voltage vector  $\mathbf{v}_\psi$  shown in the vector diagram in Fig. 7. In practice, however, the modulation index  $m$  should correspond to the amplitude of the stator voltage vector  $\mathbf{v}_s$ . Therefore, the voltage drop in the stator resistance is taken into account to adjust the value of the modulation index.

Following, in order to retrieve the switching angles and structure of the offline-computed nominal OPP  $\mathbf{p}(d, m)$  from

<sup>9</sup>The interested reader is referred to [12] and [19] for details on the derivation.

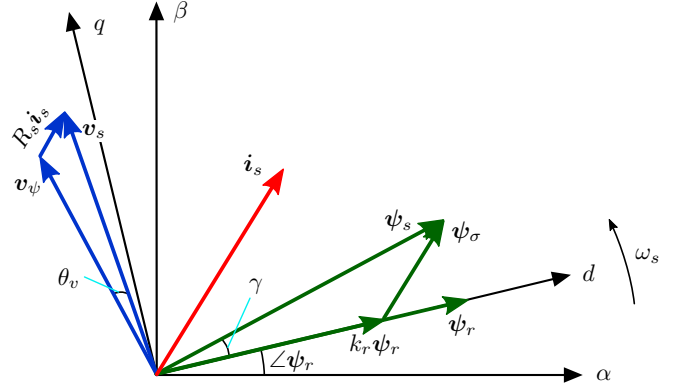


Fig. 7: Vector diagram of an induction machine.

the respective LUTs, the desired pulse number  $d$  is required. This is chosen based on the desired and/or maximum allowable device switching frequency, see [7, Section 12.4.5]. With both  $m$  and  $d$ —and thus  $\mathbf{p}(d, m)$ —the complete single-phase OPP is obtained by applying quarter-wave and half-wave symmetry, see Section III. Based on this, the three-phase OPP is constructed, and  $\omega_s$  is used to translate the switching angles into switching time instants.

**Step 1.1.** The rotor flux  $\psi_r$  is estimated based on the stator current and machine speed measurements. In doing so, the estimated rotor flux angle  $\angle\psi_r$  is acquired which is used for the compensation of the total time delay. This is realized by rotating the estimated rotor flux vector by  $\omega_s T_s$  forward in time, i.e., the angular position  $\angle\psi_r + \omega_s T_s$  is assumed. Accordingly, a one-step delay compensation is employed for the current measurements. Moreover,  $\angle\psi_r$  is used for the transformation of the outer-loop quantities from the rotating  $dq$ -frame to the stationary  $(\alpha\beta)$  one, see Fig. 6.

**Step 1.2.** The nominal OPP is shifted such that its fundamental component is correctly aligned with the stator voltage vector  $\mathbf{v}_s$ . To this end, the load angle  $\gamma$ , i.e., the angular displacement between the stator and the rotor flux vectors, needs to be computed. Recall that the electromagnetic torque can be written as [7, Section 12.4]

$$T_e = \frac{1}{\text{pf}} \frac{X_m}{D} \Psi_s \Psi_r \sin(\gamma), \quad (19)$$

where pf is the power factor of the IM. Conversely, for a given value of the torque reference  $T_{e,\text{ref}}$ , the desired load angle is

$$\gamma_{\text{ref}} = \arcsin\left(\text{pf} \frac{D}{X_m} \frac{T_{e,\text{ref}}}{\Psi_{s,\text{ref}} \Psi_{r,\text{ref}}}\right). \quad (20)$$

Therefore, the stator flux angle is  $\angle\psi_s = \angle\psi_r + \gamma_{\text{ref}}$ . By introducing a counterclockwise rotation of  $90^\circ$ , the angle of the vector  $\mathbf{v}_\psi$  is obtained (see Fig. 7). Hence, by appropriately accounting for the phase-shift  $\theta_v$  introduced by the voltage drop across the stator resistance, the angle of the stator voltage vector  $\mathbf{v}_s$  is found, and used for the correct alignment of the three-phase OPP.

**Step 2.** With the knowledge of the three-phase nominal OPP position at the discrete time step  $kT_s$ , the  $z$  nominal switching instants  $t_{i,\text{ref}}$  that fall within the prediction horizon  $T_p$  are extracted along with the corresponding switch positions  $\mathbf{u}_{abc}(t_{i,\text{ref}})$ . As explained in Section IV-B,  $z$ , i.e., the

dimension of  $\mathbf{t}_{\text{ref}}$ , defines the size of the optimization problem (i.e., the dimension of the optimization variable  $\mathbf{t}$ ) as well as the number of stator current gradients  $\mathbf{m}(t_{\ell,\text{ref}})$  that need to be computed. Note that the latter are not necessarily unique, meaning that, in practice, (significantly) less than  $z$  gradients may require computation.

**Step 3.** In this step, the optimal stator current reference trajectory  $\mathbf{i}_{s,\text{ref}}$  is computed at the nominal OPP switching time instants that fall within the prediction horizon  $T_p$ , i.e., at  $\mathbf{t}_{\text{ref}}$ . To this aim, first the fundamental component of the current reference which is provided by the outer loop in the rotating  $dq$ -frame is transformed into the stationary  $\alpha\beta$ -frame. This yields  $\mathbf{i}_{s1,\text{ref}}$ . Subsequently, the harmonic current components  $\mathbf{i}_{sh,\text{ref}}(d, m)$  are added to generate the complete reference current trajectory  $\mathbf{i}_{s,\text{ref}}$ . Moreover, to compensate for the voltage drop across the stator resistance, the current reference trajectory is phase-shifted by the angle  $\theta_v$ , as depicted in Fig. 7. As a result, the vector of the optimal stator current reference values over the prediction horizon is obtained, i.e.,  $\mathbf{Y}_{\text{ref}} = [\mathbf{i}_{s,\text{ref}}^T(t_{1,\text{ref}}) \quad \mathbf{i}_{s,\text{ref}}^T(t_{2,\text{ref}}) \quad \dots \quad \mathbf{i}_{s,\text{ref}}^T(t_{z,\text{ref}})]^T$ .

**Step 4.** Following, the matrix of current gradients  $\mathbf{M}$  is formulated, see (17) and Appendix C. To this aim, (15) is used, which computes the necessary current gradients based on the measured or estimated state, the nominal switching instants  $\mathbf{t}_{\text{ref}}$ , and the vector of nominal OPP switch positions  $\mathbf{U}$ .

**Step 5.** The optimization problem underlying GP<sup>3</sup>C is formulated in this step. Specifically, given the simplified objective function (17), the optimal control problem takes the form

$$\begin{aligned} & \underset{\mathbf{t} \in \mathbb{R}^z}{\text{minimize}} && \|\mathbf{r} - \mathbf{M}\mathbf{t}\|_2^2 + \lambda_t \|\Delta\mathbf{t}\|_2^2 \\ & \text{subject to} && kT_s < t_1 < \dots < t_z < kT_s + T_p. \end{aligned} \quad (21)$$

As can be seen in (21), the to-be-computed switching time instants cannot be modified arbitrarily; they are rather constrained such that the sequence of switching transitions of the three-phase pulse pattern is maintained. Moreover, upper and lower bounds are imposed on  $\mathbf{t}$ . More specifically, the current time instant  $kT_s$  serves as a lower bound so that the switching instants are not moved into the past, while the end of the horizon  $kT_s + T_p$  is the upper bound. Fig. 5(a) exemplifies this for the five switching instants within the prediction horizon, where the constraints on the to-be-computed switching time instants are indicated with arrows. For example, the first to-be-computed switching instant  $t_1$  is constrained by the present time instant  $kT_s$  and the *actual* second switching instant  $t_2$ . Based on the same principle, the second switching instant, i.e.,  $t_2$ , is bounded between  $t_1$  and  $t_3$ , and so on.

It is worth mentioning that since the objective function (17) is quadratic and the constraints are linear, problem (21) is a convex QP [20]. Such problems can be efficiently solved with existing off-the-self solvers, see, e.g., [8, Section IV].<sup>10</sup> The solution to the QP (21), called the *optimizer*, is the vector of the optimally modified switching time instants  $\mathbf{t}^*$ .

**Step 6.** In a last step, the required optimal modifications on the OPP switching time instants that fall within the first sampling interval of the prediction horizon, i.e., between  $kT_s$  and  $(k+1)T_s$ , are implemented. This means that the switch

Table I: Rated values of the induction machine.

Parameter	Symbol	SI Value
Voltage	$V_R$	3300 V
Current	$I_R$	356 A
Apparent power	$S_R$	2.034 MVA
Stator Frequency	$\omega_{sR}$	$2\pi 50$ rad/s
Rotational speed	$\omega_R$	596 rpm

Table II: System parameter values in the SI and the p.u. system.

Parameter	Symbol	SI value	p.u. value
Stator resistance	$R_s$	57.61 m $\Omega$	0.0108
Rotor resistance	$R_r$	48.89 m $\Omega$	0.0091
Stator leakage inductance	$X_{ls}$	2.544 mH	0.1493
Rotor leakage inductance	$X_{lr}$	1.881 mH	0.1104
Mutual inductance	$X_m$	40.014 mH	2.3489
Dc-link voltage	$V_{dc}$	5.2 kV	1.9299
Dc-link capacitance	$X_{dc}$	2.238 mF	3.7628

positions of the OPP  $\mathbf{u}_{abc}$  are to be applied to the converter at the computed time instants  $\mathbf{t}^*$ .

Finally, according to the receding horizon policy of MPC [7], the horizon is shifted by one  $T_s$ , and the procedure begins from “Step 0” based on new measurements or estimates and an updated OPP.<sup>11</sup> In doing so, feedback is provided to the controller, and a high degree of robustness to system non-idealities, such as persistent harmonics due to a significant dc-link voltage ripple, is achieved, as shown in the following section, where the performance of GP<sup>3</sup>C is assessed.

**Example 3:** Consider the nominal OPP in Fig. 5(a). By applying this OPP to the converter the (linearized) evolution of the stator current is shown as a dash-dotted (magenta) line. The OPP is to be manipulated by GP<sup>3</sup>C such that the stator current tracks the (sampled) optimal reference trajectory shown with a dashed (black) line. To this end, the controller modifies the five OPP switching time instants  $t_{1,\text{ref}} - t_{5,\text{ref}}$  that fall within  $T_p$ . The modified time instants  $t_1 - t_5$ , shown in Fig. 5(b), result in the stator current shown as solid (green) line. The volt-second corrections in the three-phases are indicated by arrows and highlighted in yellow. For example, the volt-second area in phase  $c$  is increased by  $\Delta t_1$ , whereas the volt-second area in phase  $a$  is decreased by  $\Delta t_2$ . The (modified) pattern that falls within the first sampling interval  $T_s$ —shown in red in Fig. 5(b)—is applied to the inverter and the horizon is shifted by one  $T_s$ . ■

#### D. Flux Estimation

As shown in the block diagram in Fig. 6, the outer loop, designed in the  $dq$ -reference frame, resembles a field-oriented controller where the speed and the flux controllers are based on PI controllers [7, Section 3.6]. To achieve field orientation, the rotor flux angle needs to be estimated. By using the measured stator current and the stator voltage<sup>12</sup> the rotor flux vector can

<sup>11</sup>After implementing the modifications that fall within  $T_s$ , the OPP in use is updated accordingly, i.e., by removing any switching transitions that have been applied to the inverter.

<sup>12</sup>Typically, the stator voltage is not measured but rather reconstructed based on the dc-link voltage and the (known) applied pulse pattern.

<sup>10</sup>The real-time solution of (21) is discussed in [13].

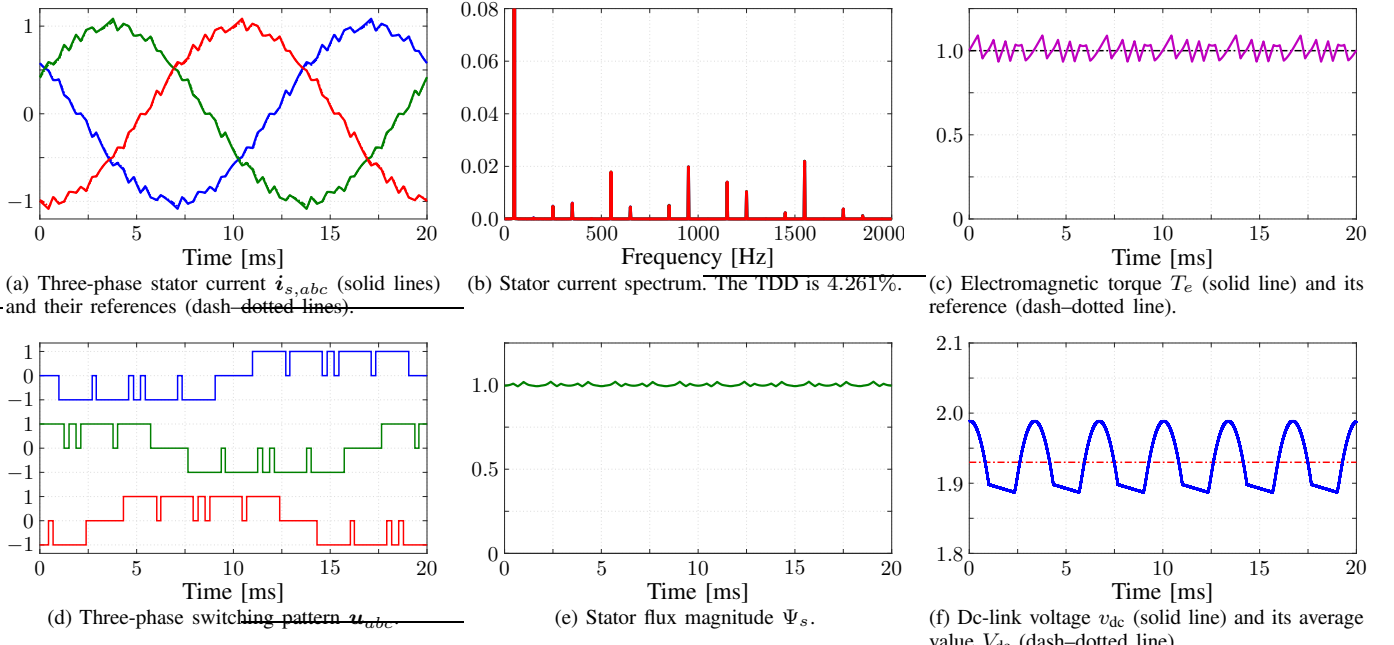


Fig. 8: Simulation results produced by the proposed GP<sup>3</sup>C algorithm at steady-state operation, nominal speed and rated torque. The modulation index is  $m = 1.046$ , the pulse number is  $d = 5$ , and the switching frequency is 250 Hz.

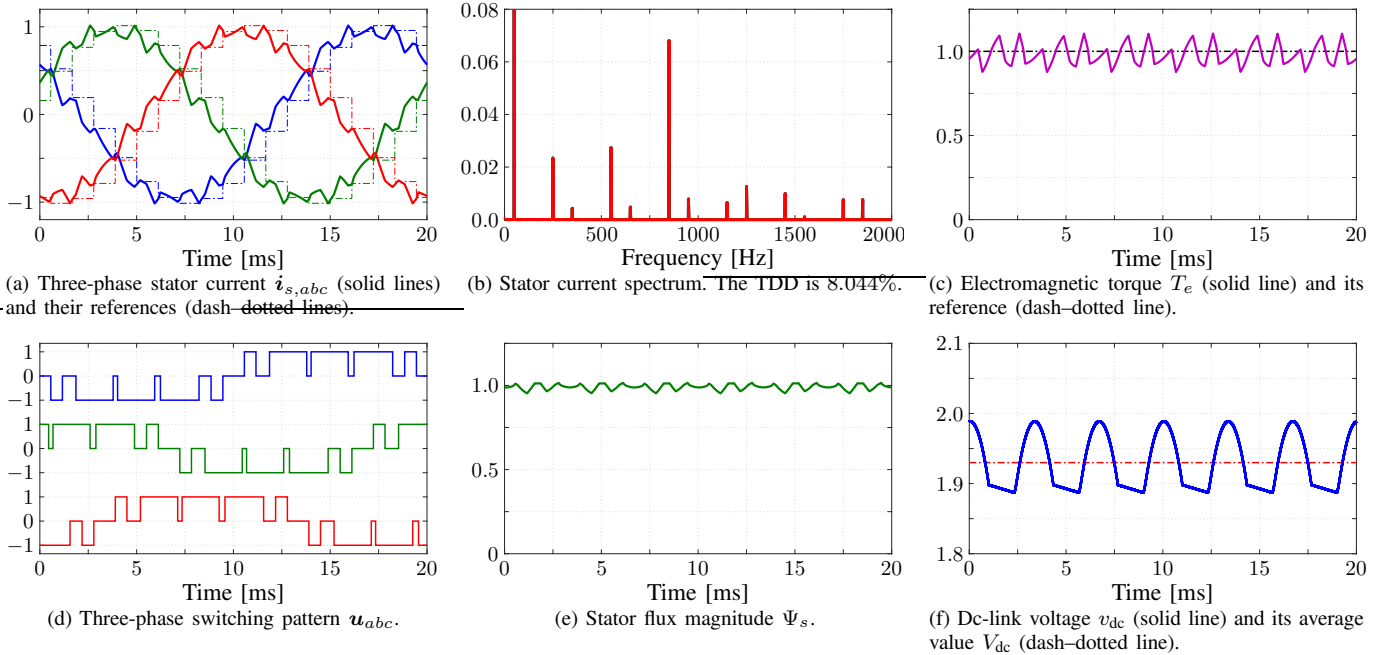


Fig. 9: Simulation results produced by FOC with SVM at steady-state operation, nominal speed and rated torque. The switching frequency is 250 Hz.

be estimated. With (2) and (3), the rotor flux vector can be calculated as

$$\psi_r(t) = \frac{X_r}{X_m} \int_0^{T_s} \left( \frac{v_{dc}}{2} \mathbf{u}_{abc} - R_s \mathbf{i}_s \right) dt - \frac{\sigma X_s X_r}{X_m} \mathbf{i}_s, \quad (22)$$

where  $\sigma = 1 - X_m^2 / (X_r X_s)$  is the total leakage factor. From (22), it directly follows that the magnitude of the rotor flux is  $\Psi_r = \|\psi_r\|$  and its angular position  $\angle \psi_r = \arctan\left(\frac{\psi_{r\beta}}{\psi_{r\alpha}}\right)$ . Note that the accuracy of the flux estimation (22) is typically improved by incorporating it in an

observer [21]. To this aim, the system dynamics are augmented with a correction term, i.e., the feedback of the error between the actual output of the system and that of its model. By scaling this error with the observer gain the estimated flux value converges to its correct value.

## V. PERFORMANCE EVALUATION

The performance of the proposed GP<sup>3</sup>C scheme for the drive shown in Fig. 1 is evaluated in this section by simulations. It is assumed that the IM has a constant mechanical load.

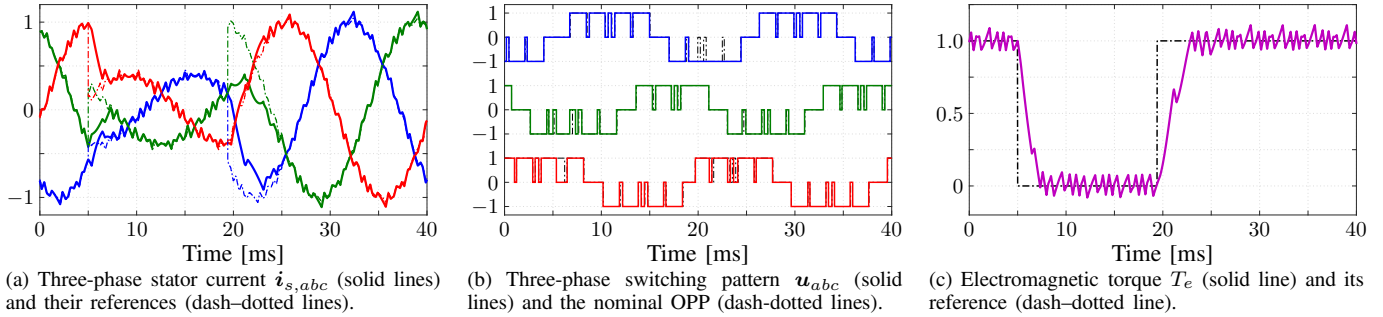


Fig. 10: Simulation results produced by the proposed GP<sup>3</sup>C algorithm during torque reference steps. The pulse number is  $d = 5$ .

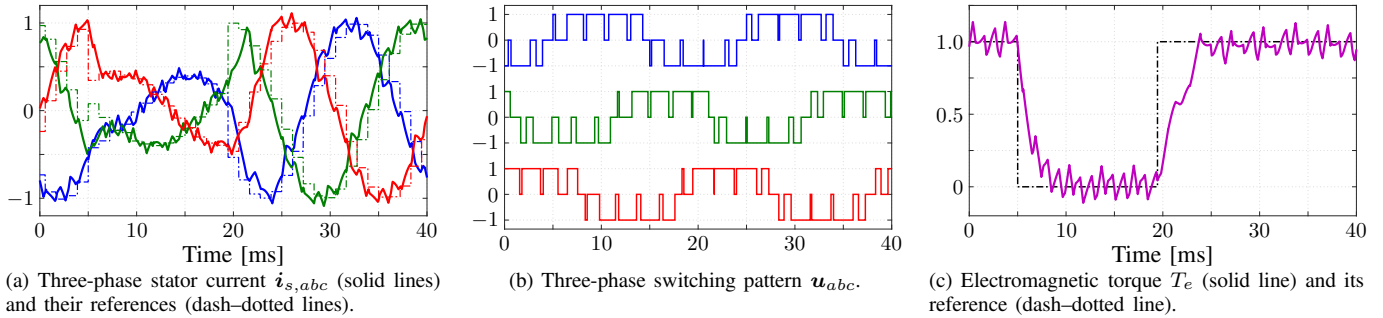


Fig. 11: Simulation results produced by FOC with SVM during torque reference steps.

The rated parameters of the machine are given in Table I. Based on the drive parameters provided in Table II it can be deduced that the IM has a total leakage reactance of  $X_\sigma = 0.255$  p.u. Moreover, it is worth mentioning that the average dc-link voltage of the inverter—supplied by diode rectifiers, as shown in Fig. 1—is  $V_{dc} = 5.2$  kV, while its peak-to-peak ripple is about 234 V. The tested OPP has a pulse number of  $d = 5$ , while the modulation index is  $m = 1.046$ . For the presented simulations the sampling interval is set to  $T_s = 50$   $\mu$ s and a 25-step prediction horizon (i.e.,  $N_p = 25$ ) is chosen. The weighting factor on the manipulated variable is  $\lambda_t = 4 \cdot 10^5$ . Note that all results in the sequel of this section are presented in the p.u. system.

#### A. Steady-State Performance

First, the steady-state performance of the MV drive system is examined for operation at rated torque and nominal speed. The latter implies that the device switching frequency is 250 Hz since  $d = 5$ . The corresponding results of GP<sup>3</sup>C are presented in Fig. 8. The three-phase stator current is shown over one fundamental period in Fig. 8(a). As can be seen, the current reference tracking performance of the controller is excellent, with only minute deviations from the optimal trajectory being observed. This occurs despite the strong dc-link voltage ripple (see Fig. 8(f)), indicating the ability of the controller to successfully deal with external disturbances. As a result, the harmonic distortions are very low, as indicated by the current TDD  $I_{TDD}$  of 4.261%. Moreover, thanks to the symmetry properties of the nominal OPP, which are preserved—to some extent—by the controller (see Fig. 8(d) for the three-phase switching pattern generated by the controller), the harmonic power is concentrated at frequencies which

are odd, non-triplen integer multiples of the fundamental. Furthermore, owing to the good current reference tracking, the electromagnetic torque also accurately tracks its reference, see Fig. 8(c). Finally, Fig. 8(e) shows the stator flux magnitude.

To clearly demonstrate the superior steady-state performance of GP<sup>3</sup>C, it is benchmarked with FOC with SVM. The latter is implemented as three-level asymmetric regularly sampled CB-PWM with common-mode signal injection of the min/max type to resemble SVM [22]. The PI controllers of FOC are tuned based on the modulus optimum method, while the switching frequency is also 250 Hz to ensure a fair comparison with GP<sup>3</sup>C. Fig. 9 depicts the steady-state behavior of the drive controlled by FOC. As can be observed, this is inferior to that of GP<sup>3</sup>C as the stator current has a significantly higher current ripple, see Fig. 9(a). The lower quality of the current is not only quantified by the higher—almost double—current TDD  $I_{TDD}$  of 8.044%, but it is also visualized in the harmonic spectrum presented in Fig. 9(b). Therein, it can be seen that the harmonic power is higher, especially at low frequencies. Low-frequency harmonics, such as the 5<sup>th</sup> and 7<sup>th</sup>, are also amplified due to the dc-link voltage ripple at 300 Hz, suggesting that FOC cannot reject this external disturbance as effectively as GP<sup>3</sup>C can.

#### B. Transient Performance

The transient performances of the proposed GP<sup>3</sup>C scheme and FOC are presented in Figs. 10 and 11, respectively. For the presented cases, operation at nominal speed is considered, while the torque reference is stepped down from 1 to 0 p.u. at  $t = 5$  ms, and stepped back to 1 p.u. at  $t = 20$  ms. Despite the big changes in the torque reference, GP<sup>3</sup>C manages to quickly settle to the new operating points by significantly modifying

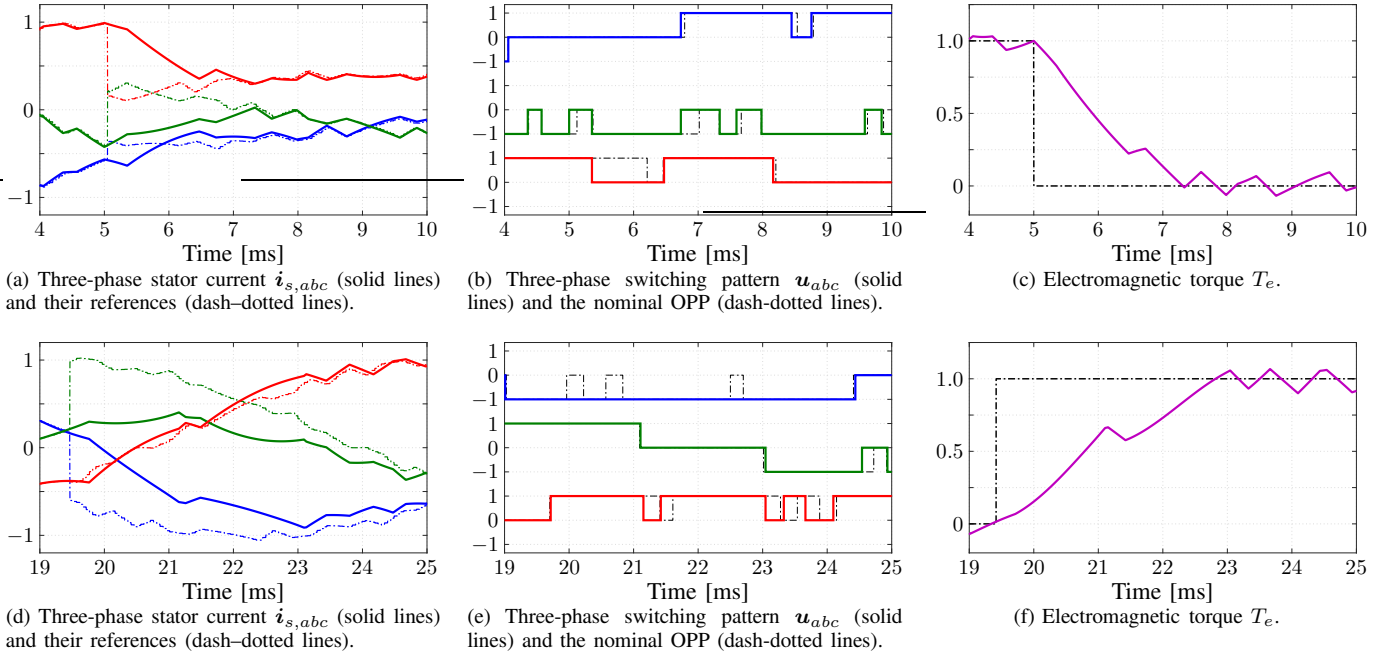


Fig. 12: Transient performance of GP<sup>3</sup>C at rated speed during a torque reference (a)–(c) step-down change, and (d)–(f) step-up change (zoomed in). In (b) and (e), the (black) dash-dotted lines refer to the switching sequence of the unmodified, nominal OPP, whereas the solid lines correspond to the modified switching sequence as computed by GP<sup>3</sup>C.

the nominal OPP, see Fig. 12. Specifically, during the torque reference step-down change, the proposed controller applies the switch positions that will decrease the load angle as fast as possible, as Fig. 12 shows in detail. As can be seen in Fig. 12(b), this is done by significantly reducing the width of the pulses in phase  $c$  and by shifting forward in time the pulses in phases  $a$  and  $b$ . The same observations can be made for the step-up case, as illustrated in more detail in Fig. 12(e). It is noteworthy that in this scenario GP<sup>3</sup>C completely removes pulses from phase  $a$ , such that the available dc-link voltage is fully utilized.

On the other hand, FOC with SVM does not achieve such short settling times, see Fig. 11. Even though the FOC current control loop is designed such that it has a high bandwidth—as the PI controllers are tuned based on the modulus optimum method—the transient performance is inferior to that of GP<sup>3</sup>C. This can be explained by the fact that the controller and modulator—FOC and SVM, respectively—are two decoupled entities that act independently from each other, i.e., in an uncoordinated manner. As a result, the dynamic behavior of the closed-loop system is compromised. This is in stark contrast to the operational principle of GP<sup>3</sup>C, which, as a direct control method, formulates the control and modulation problems in one computational stage, thus avoiding limitations imposed by a dedicated modulator.

## VI. CONCLUSIONS

This paper proposed a control and modulation scheme for MV drive systems that employs MPC and OPPs. By using the stator current gradients to serve as a simple, yet accurate enough prediction model, the optimal control problem formulation is greatly simplified, and a high degree of design

versatility is achieved. Moreover, thanks to the adopted prediction model, the optimization problem underlying direct MPC is cast as a convex QP, thus requiring only modest computational resources. As a result, the real-time implementation of the proposed control and modulation scheme is rendered feasible, as shown in [13], where GP<sup>3</sup>C is tested in real time in a hardware-in-the-loop environment. More importantly, as the proposed strategy is a combination of an optimal constrained controller with an optimal modulation technique, superior steady-state and transient performance can be achieved, as verified with the presented results. The former is credited to the inherent feature of OPPs to produce the lowest possible current distortions at a given switching frequency. Furthermore, owing to the characteristics of the proposed control and modulation scheme, such as the long horizon and the receding horizon policy, a significant degree of robustness to system non-idealities, e.g., dc-link voltage ripples, is provided. As for the dynamic behavior of the controller, the direct control nature of GP<sup>3</sup>C, combined with its ability to modify the nominal OPPs in an optimal manner, allow for very short settling times. As shown in the paper, thanks to these features, GP<sup>3</sup>C can outperform conventional control methods, such as FOC with SVM.

## APPENDIX A CONTINUOUS-TIME SYSTEM MATRICES

The matrices of the continuous-time state-space model in (5) are

$$F = \begin{bmatrix} -\frac{1}{\tau_s} & 0 & \frac{X_m}{\tau_r D} & \omega_r \frac{X_m}{D} \\ 0 & -\frac{1}{\tau_s} & -\omega_r \frac{X_m}{D} & \frac{X_m}{\tau_r D} \\ \frac{X_m}{\tau_r} & 0 & -\frac{1}{\tau_r} & -\omega_r \\ 0 & \frac{X_m}{\tau_r} & \omega_r & -\frac{1}{\tau_r} \end{bmatrix},$$

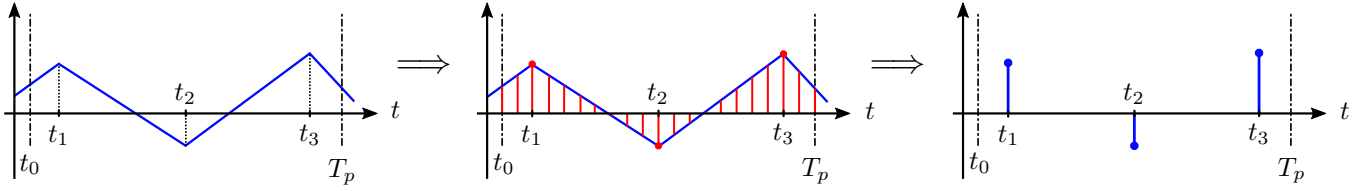


Fig. 13: Approximation of the rms error signal.

$$\mathbf{G} = \frac{v_{dc} X_r}{2 D} \begin{bmatrix} 1 & 0 \\ 0 & 1 \\ 0 & 0 \\ 0 & 0 \end{bmatrix} \mathbf{K}, \quad \mathbf{C} = \begin{bmatrix} 1 & 0 & 0 & 0 \\ 0 & 1 & 0 & 0 \end{bmatrix}.$$

#### APPENDIX B

##### APPROXIMATION OF THE RMS ERROR

The first term in (11) captures the (squared) rms error of the stator current within the horizon  $T_p$ , i.e.,

$$J_1 = \frac{1}{T_p} \left( \int_0^{T_p} \|\mathbf{i}_{s,\text{err}}(t)\|_2^2 dt \right), \quad (23)$$

where  $\mathbf{i}_{s,\text{err}}(t) = \mathbf{i}_{s,\text{ref}}(t) - \mathbf{i}_s(t)$ . The rms value of the continuous-time signal in (23) can be accurately approximated by the rms value of the equivalent (regularly sampled) discrete-time signal  $\mathbf{i}_{s,\text{err}}(n)$

$$J_1 = \frac{1}{N} \sum_{n=0}^{N-1} \|\mathbf{i}_{s,\text{err}}(n)\|_2^2, \quad (24)$$

provided that a sufficient number of samples  $N \in \mathbb{N}^+$  is considered.

Analyzing (24), two interesting observations can be made. First, the objective function term  $J_1$  is a quadratic function of time. This is in contrast to the  $J_1$  in (23), which is a cubic function of time. Thanks to this, (24) leads to a convex optimization problem, as opposed to the nonconvex problem resulting from (23). This is advantageous from optimization perspective, as convex problems are relatively easy to solve.

For the second observation, we invoke Parseval's theorem which states that for a discrete-time signal  $\chi$  of  $N$  samples it holds that [23]

$$\sum_{n=0}^{N-1} |\chi(n)|^2 = \frac{1}{N} \sum_{m=0}^{N-1} |\mathbf{X}(m)|^2, \quad (25)$$

where  $\mathbf{X}$  is the discrete Fourier transform (DFT) of  $\chi$ . This implies that the total energy of a signal can be calculated by summing the power-per-sample across time or the spectral power across frequency [23]. Therefore, the total energy captured by (24) is equivalent to the harmonic distortions of the stator current within the prediction horizon. Hence, as also shown in [24, Appendix A], minimizing (24) is equivalent to minimizing the stator current TDD over the prediction horizon  $T_p$ .

From the above it can be concluded that using (24) to represent the current reference tracking term is an excellent choice as it can lead to favorable performance (low current TDD) and a convex optimization problem. Nevertheless, as

discussed in [12], using regularly-spaced samples may lead to an unnecessarily complicated optimization problem that will require more computational resources to solve in real time. To avoid this, the sampled current error can be coarsely approximated by using a finite number of irregularly spaced samples as depicted, e.g., in Fig. 13. Given that the switching time instants of the OPP that fall within the prediction horizon are known, the simplest approach is to penalize the deviation of the stator current from its reference only at the OPP switching instants. This yields

$$J_1 = \frac{1}{z} \sum_{n=1}^z \|\mathbf{i}_{s,\text{err}}(n)\|_2^2, \quad (26)$$

where  $z$  is the number of switching instants that fall within  $T_p$ . The function (26) provides a very coarse approximation of the rms error, which is nevertheless often quite effective. Hence, the objective function given in (12) uses (26) as the current reference tracking term, where the scaling factor  $1/z$  is integrated into  $\lambda_t$ .

#### APPENDIX C

##### DESCRIPTION OF THE OBJECTIVE FUNCTION

The vector  $\mathbf{r}$  and matrix  $\mathbf{M}$  in (17) are

$$\mathbf{r} = \begin{bmatrix} \mathbf{i}_{s,\text{ref}}(t_{1,\text{ref}}) - \mathbf{i}_s(t_0) \\ \mathbf{i}_{s,\text{ref}}(t_{2,\text{ref}}) - \mathbf{i}_s(t_0) \\ \mathbf{i}_{s,\text{ref}}(t_{3,\text{ref}}) - \mathbf{i}_s(t_0) \\ \vdots \\ \mathbf{i}_{s,\text{ref}}(t_{z,\text{ref}}) - \mathbf{i}_s(t_0) \end{bmatrix}$$

and

$$\mathbf{M} = \begin{bmatrix} \mathbf{m}_{t_0} & \mathbf{0}_2 & \mathbf{0}_2 & \dots & \mathbf{0}_2 & \mathbf{0}_2 \\ \mathbf{m}_0 & \mathbf{m}_{t_1} & \mathbf{0}_2 & \dots & \mathbf{0}_2 & \mathbf{0}_2 \\ \mathbf{m}_0 & \mathbf{m}_1 & \mathbf{m}_{t_2} & \dots & \mathbf{0}_2 & \mathbf{0}_2 \\ \vdots & \vdots & \vdots & \ddots & \vdots & \vdots \\ \mathbf{m}_0 & \mathbf{m}_1 & \mathbf{m}_2 & \dots & \mathbf{m}_{t_{z-2}} & \mathbf{0}_2 \\ \mathbf{m}_0 & \mathbf{m}_1 & \mathbf{m}_2 & \dots & \mathbf{m}_{z-2} & \mathbf{m}_{t_{z-1}} \end{bmatrix}$$

with

$$\begin{aligned} \mathbf{m}_{t_\ell} &= \mathbf{m}(t_{\ell,\text{ref}}) \\ \mathbf{m}_\ell &= \mathbf{m}(t_{\ell,\text{ref}}) - \mathbf{m}(t_{\ell+1,\text{ref}}) \end{aligned}$$

where  $\ell \in \{0, 1, 2, \dots, z-1\}$ .

#### REFERENCES

- [1] G. S. Buja, "Optimum output waveforms in PWM inverters," *IEEE Trans. Ind. Appl.*, vol. IA-16, no. 6, pp. 830–836, Nov./Dec. 1980.

- [2] J. Holtz and B. Beyer, "Optimal synchronous pulsewidth modulation with a trajectory-tracking scheme for high-dynamic performance," *IEEE Trans. Ind. Appl.*, vol. 29, no. 6, pp. 1098–1105, Nov./Dec. 1993.
- [3] —, "Fast current trajectory tracking control based on synchronous optimal pulsewidth modulation," *IEEE Trans. Ind. Appl.*, vol. 31, no. 5, pp. 1110–1120, Sep./Oct. 1995.
- [4] —, "The trajectory tracking approach—a new method for minimum distortion PWM in dynamic high-power drives," *IEEE Trans. Ind. Appl.*, vol. 30, no. 4, pp. 1048–1057, Aug. 1994.
- [5] N. Oikonomou and J. Holtz, "Stator flux trajectory tracking control for high-performance drives," in *Conf. Rec. of the IEEE Ind. Appl. Soc. Annu. Meet.*, vol. 3, Tampa, FL, Oct. 2006, pp. 1268–1275.
- [6] J. Holtz and N. Oikonomou, "Synchronous optimal pulsewidth modulation and stator flux trajectory control for medium-voltage drives," *IEEE Trans. Ind. Appl.*, vol. 43, no. 2, pp. 600–608, Mar./Apr. 2007.
- [7] T. Geyer, *Model Predictive Control of High Power Converters and Industrial Drives*. Hoboken, NJ, USA: Wiley, 2016.
- [8] P. Karamanakos, E. Liegmann, T. Geyer, and R. Kennel, "Model predictive control of power electronic systems: Methods, results, and challenges," *IEEE Open J. Ind. Appl.*, vol. 1, pp. 95–114, 2020.
- [9] T. Geyer, N. Oikonomou, G. Papafotiou, and F. D. Kieferndorf, "Model predictive pulse pattern control," *IEEE Trans. Ind. Appl.*, vol. 48, no. 2, pp. 663–676, Mar./Apr. 2012.
- [10] N. Oikonomou, C. Gutscher, P. Karamanakos, F. D. Kieferndorf, and T. Geyer, "Model predictive pulse pattern control for the five-level active neutral-point-clamped inverter," *IEEE Trans. Ind. Appl.*, vol. 49, no. 6, pp. 2583–2592, Nov./Dec. 2013.
- [11] T. Geyer, V. Spudić, W. van der Merwe, and E. Guidi, "Model predictive pulse pattern control of medium-voltage neutral-point-clamped inverter drives," in *Proc. IEEE Energy Convers. Congr. Expo.*, Portland, OR, USA, Sep. 2018, pp. 5047–5054.
- [12] P. Karamanakos, R. Mattila, and T. Geyer, "Fixed switching frequency direct model predictive control based on output current gradients," in *Proc. IEEE Ind. Electron. Conf.*, Washington, D.C., USA, Oct. 2018, pp. 2329–2334.
- [13] M. A. W. Begh, P. Karamanakos, T. Geyer, and Q. Yang, "Gradient-based predictive pulse pattern control of medium-voltage drives—Part II: Performance assessment," *IEEE Trans. Power Electron.*, 2022, in press.
- [14] J. Holtz, "The representation of ac machine dynamics by complex signal flow graphs," *IEEE Trans. Ind. Electron.*, vol. 42, no. 3, pp. 263–271, Jun. 1995.
- [15] P. C. Krause, O. Wasynczuk, S. D. Sudhoff, and S. D. Pekarek, *Analysis of electric machinery and drive systems*. Hoboken, NJ, USA: John Wiley & Sons, 2013.
- [16] A. Birth, T. Geyer, H. Mouton, and M. Dorfling, "Generalized three-level optimal pulse patterns with lower harmonic distortion," *IEEE Trans. Power Electron.*, vol. 35, no. 6, pp. 5741–5752, Jun. 2020.
- [17] A. K. Rathore, J. Holtz, and T. Boller, "Synchronous optimal pulsewidth modulation for low-switching-frequency control of medium-voltage multilevel inverters," *IEEE Trans. Ind. Electron.*, vol. 57, no. 7, pp. 2374–2381, Jul. 2010.
- [18] G. S. Buja and G. B. Indri, "Optimal pulsewidth modulation for feeding ac motors," *IEEE Trans. Ind. Appl.*, vol. IA-13, no. 1, pp. 38–44, Jan. 1977.
- [19] P. Karamanakos, M. Nahalparvari, and T. Geyer, "Fixed switching frequency direct model predictive control with continuous and discontinuous modulation for grid-tied converters with *LCL* filters," *IEEE Trans. Control Sys. Technol.*, vol. 29, no. 4, pp. 1503–1518, Jul. 2021.
- [20] S. Boyd and L. Vandenberghe, *Convex optimization*. Cambridge, UK: Cambridge Univ. Press, 2004.
- [21] G. C. Verghese and S. R. Sanders, "Observers for flux estimation in induction machines," *IEEE Trans. Ind. Electron.*, vol. 35, no. 1, pp. 85–94, Feb. 1988.
- [22] B. P. McGrath, D. G. Holmes, and T. Lipo, "Optimized space vector switching sequences for multilevel inverters," *IEEE Trans. Power Electron.*, vol. 18, no. 6, pp. 1293–1301, Nov. 2003.
- [23] A. V. Oppenheim and R. W. Schaffer, *Discrete-time signal processing*. Essex, UK: Pearson Edu. Ltd., 2014.
- [24] T. Geyer, "Algebraic tuning guidelines for model predictive torque and flux control," *IEEE Trans. Ind. Appl.*, vol. 54, no. 5, pp. 4464–4475, May 2018.



**Mirza Begh** (S'19) received the B.Tech. degree in electrical engineering from NIT Hamirpur, Hamirpur, India in 2014, and M.Sc. degree in electrical power engineering from Technische Universität München (TUM), Munich, Germany, in 2018. Since 2019, he has been pursuing the Ph.D. degree in electrical engineering at the Faculty of Information Technology and Communication Sciences, Tampere University, Tampere, Finland.

From 2014 to 2015 he was with the ABB Global R&D Centre, Bangalore, India, where he worked on the testing of low-voltage drives and PLCs. From 2015 to 2016 he was working as a University Lecturer at the Institute of Technology, University of Kashmir, Srinagar, India. In 2018, he was with the Fraunhofer Institute for Solar Energy Systems (ISE) where he worked on the design of control methods for grid-connected systems. His research interests include power electronics and electrical drives, optimal control, and optimal modulation methods.

Mr. Begh was the recipient of the Student Attendance Grant at the 2021 IEEE Energy Conversion Congress and Exposition.



**Petros Karamanakos** (S'10–M'14–SM'19) received the Diploma and Ph.D. degrees in electrical and computer engineering from the National Technical University of Athens (NTUA), Athens, Greece, in 2007, and 2013, respectively.

From 2010 to 2011 he was with the ABB Corporate Research Center, Baden-Dättwil, Switzerland, where he worked on model predictive control strategies for medium-voltage drives. From 2013 to 2016 he was a PostDoc Research Associate in the Chair of Electrical Drive Systems and Power Electronics, Technische Universität München, Munich, Germany. Since 2016, he has been with the Faculty of Information Technology and Communication Sciences, Tampere University, Tampere, Finland, where he is currently an Associate Professor. His main research interests lie at the intersection of optimal control, mathematical programming and power electronics, including model predictive control and optimal modulation for power electronic converters and ac variable speed drives.

Dr. Karamanakos received the 2014 Third Best Paper Award of the IEEE Transactions on Industry Applications and two Prize Paper Awards at conferences. He serves as an Associate Editor of the IEEE Transactions on Industry Applications and of the IEEE Open Journal of Industry Applications. He is a Regional Distinguished Lecturer of the IEEE Power Electronics Society in the years 2022 and 2023.



**Tobias Geyer** (M'08–SM'10–F'22) received the Dipl.-Ing. degree in electrical engineering, the Ph.D. in control engineering, and the Habilitation degree in power electronics from ETH Zurich in the years 2000, 2005, and 2017, respectively.

After his Ph.D., he spent three years at GE Global Research, Munich, Germany, three years at the University of Auckland, Auckland, New Zealand, and eight years at ABB's Corporate Research Centre, Baden-Dättwil, Switzerland. In 2020, he joined ABB's Medium-Voltage Drive division as R&D platform manager of the ACS6080. In 2022, he became a Corporate Executive Engineer. Working at the intersection of industry and academia he is also an extraordinary Professor at Stellenbosch University, Stellenbosch, South Africa, from the year 2017 until 2023.

He is the author of more than 35 patent families, 150 publications and the book "Model predictive control of high-power converters and industrial drives" (Wiley, 2016). He teaches a regular course on model predictive control at ETH Zurich. His research interests include medium-voltage and low-voltage drives, utility-scale power converters, optimized pulse patterns and model predictive control.

Dr. Geyer received the PELS Modeling and Control Technical Achievement Award in 2022, the Semikron Innovation Award in 2021, and the Nagamori Award in 2021. He also received two Prize Paper Awards of IEEE transactions and two Prize Paper Awards at IEEE conferences. He is a former Associate Editor of the IEEE Transactions on Industry Applications (from 2011 until 2014) and the IEEE Transactions on Power Electronics (from 2013 until 2019). He was an International Program Committee Vice Chair of the IFAC conference on Nonlinear Model Predictive Control in Madison, WI, USA, in 2018. Dr. Geyer is a Distinguished Lecturer of the IEEE Power Electronics Society from the year 2020 until 2023.